Faraday Discussions

Cite this: DOI: 10.1039/c5fd00023h

PAPER

Improved electrochemical stability at the surface of $La_{0.8}Sr_{0.2}CoO_3$ achieved by surface chemical modification

Nikolai Tsvetkov,[ab] Qiyang Lu[ac] and Bilge Yildiz*[abc]

Received 15th February 2015, Accepted 9th April 2015
DOI: 10.1039/c5fd00023h

The degradation of the surface chemistry on perovskite (ABO_3) oxides is a critical issue for their performance in energy conversion systems such as solid oxide fuel/electrolysis cells and in splitting of H_2O and CO_2 to produce fuels. This degradation is typically in the form of segregation and phase separation of dopant cations from the A-site, driven by elastic and electrostatic energy minimization and kinetic demixing. In this study, deposition of Ti at the surface was found to hinder the dopant segregation and the corresponding electrochemical degradation on a promising SOFC cathode material, $La_{0.8}Sr_{0.2}CoO_3$ (LSC). The surface of the LSC films was modified by Ti (denoted as LSC-T) deposited from a $TiCl_4$ solution. The LSC and LSC-T thin films were investigated by electrochemical impedance spectroscopy, nano-probe Auger electron spectroscopy, and X-ray photoelectron spectroscopy (XPS), upon annealing at 420–530 °C in air up to about 90 hours. The oxygen exchange coefficient, k^q, on LSC-T cathodes was found to be up to 8 times higher than that on LSC cathodes at 530 °C and retained its stability. Sr-rich insulating particles formed at the surface of the annealed LSC and LSC-T films, but with significantly less coverage of such particles on the LSC-T. From this result, it appears that modification of the LSC surface with Ti reduces the segregation of the blocking Sr-rich particles at the surface, and a larger area on LSC surface (with a higher Sr doping level in the lattice) is available for the oxygen reduction reaction. The stabilization of the LSC surface through Ti-deposition can open a new route for designing surface modifications on perovskite oxide electrodes for high temperature electro- and thermo-chemical applications.

Introduction

The surface chemical composition of functional oxides is an important factor that determines the surface reaction kinetics and affects the performance in multiple

[a]*Laboratory for Electrochemical Interfaces, Massachusetts Institute of Technology, 77 Massachusetts Avenue, Cambridge, Massachusetts 02139, USA. E-mail: byildiz@mit.edu*

[b]*Department of Nuclear Science and Engineering, Massachusetts Institute of Technology, 77 Massachusetts Avenue, Cambridge, Massachusetts 02139, USA*

[c]*Department of Material Science and Engineering, Massachusetts Institute of Technology, 77 Massachusetts Avenue, Cambridge, Massachusetts 02139, USA*

applications, including solid oxide fuel and electrolysis cells (SOFCs, SOECs),[1–11] thermochemical splitting of H_2O and CO_2,[12] oxygen permeation membranes,[13,14] batteries,[15–18] magnetic,[19–22] and catalytic[23,24] devices. For SOFC and SOEC applications, cation composition on perovskite oxide surfaces governs the reactivity and stability for oxygen reduction (ORR) and oxygen evolution (OER) reactions.[1–3,5,6,8–10,25,26] Thus, to achieve SOFCs and SOECs with high energy conversion efficiencies and long-term durability, it is important to design surfaces that are highly reactive to these reactions and have high stability. The mixed ionic and electronic conducting cobaltites, including $La_{1-x}Sr_xCoO_3$, $La_{1-x}Sr_xCo_{1-y}Fe_yO_3$ and $Ba_{1-x}Sr_xCo_{1-y}Fe_yO_3$ perovskite oxides, are state-of-the-art cathode materials which have been intensely studied and optimized to enhance the oxygen transport kinetics and surface exchange kinetics at intermediate temperatures.[27–29] One of the most promising materials is $La_{0.6}Sr_{0.4}CoO_3$, which has a very low area specific resistance (ASR) of 0.01 Ohm cm^2 at 600 °C.[27] However, recent work has shown that the surface of such perovskite oxides is not stable and undergoes segregation and phase separation of dopant oxides, typically at temperatures above 400 °C.[30–32] Similar chemical degradation of perovskite oxide surfaces was observed also for other applications of these materials, such as in magnetism,[33,34] superconductors[35] or memristors.[36,37] The consequence of such surface chemical degradation can be severe; for example, on $La_{0.6}Sr_{0.4}CoO_3$ thin film cathodes the polarization resistance of the surface was found to increase by up to 2 orders of magnitude within 50 hours at 550 °C,[9,29] correlated with the segregation and separation of SrO-related insulating phases at the surface.[7,34,38–40]

Several recent studies have attempted to prevent the surface segregation and electrochemical degradation in SOFC cathodes.[41–43] One of the proposed ways is the coating of $La_{0.8}Sr_{0.2}CoO_3$ (ref. 37) or $La_{0.6}Sr_{0.4}Co_{0.2}Fe_{0.8}O_3$ (ref. 41) electrodes with $La_{0.8}Sr_{0.2}MnO_3$. It was also shown that coating of the $La_{0.8}Sr_{0.2}CoO_3$ surface with a 5 nm thick ZrO_2 layer helps to stabilize the surface and improve electrochemical performance.[41] However the exact mechanisms on how these surface modifications improve the cathode stability have not yet been made clear, making it difficult to go beyond these empirical observations.

In our recent work, we have shown that the key driving forces behind dopant segregation at perovskite oxide surfaces are the elastic and electrostatic interactions of the dopant with the surrounding lattice.[32] The size mismatch between the dopant and host cations and the associated elastic energy minimization push the larger or smaller dopants to free surfaces or interfaces.[21,22,44,45] On the other hand, oxygen vacancies and the net positive charge at the surface of perovskite oxides[46] drive the negatively charged dopants in the form of point defects, such as Sr'_{La} or Ba'_{La}, to the surface. Based on our understanding of these two key mechanisms, we propose that the secondary phase segregation can be hindered by choosing suitable dopants. The total elastic energy driver can be minimized by a dopant that is similar in size to the host; for example, La on the La site was shown to minimize the surface segregation on $LaMnO_3$ cathode films.[32]

To minimize the electrostatic driver to the surface, the excess positive charge of the surface must be reduced. While the oxygen vacancies at the surface are important in determining the total reactivity to ORR,[47] they also contribute to attracting the aliovalent dopants, such as Sr'_{La} or Ba'_{La} defects, to the surface. This paper aims to test the hypothesis that decreasing the reducibility of the surface (thereby, reducing the concentrating of positively charged oxygen vacancies at the

surface) can decrease the amount of Sr segregation and formation of blocking SrO-related phases. We modify the $La_{0.2}Sr_{0.8}CoO_3$ (LSC) film surfaces with a small amount of Ti deposited from a chemical bath at room temperature.[48–50] These films are denoted as LSC-T in this paper. We found that both the surface chemical stability and the electrochemical performance of the LSC-T films were superior compared to the unmodified LSC films. We propose that Ti-modification of the surface is one candidate for enabling better electrochemical performance and stability on cobaltite based ORR or OER electrodes. We believe that the enhanced stability of the LSC-T cathodes is due to the weakening of the electrostatic attraction of the to the surface. Indeed, the vacancy formation energy in Ti-oxides[51] is significantly higher than in LSC.[52] Other surface compositions to modulate the surface electrostatic driving force to segregation are currently being investigated systematically in our ongoing work.

Experimental

Dense LSC films were deposited onto substrates using a pulsed laser deposition (PLD) method with a KrF excimer laser of 248 nm wavelength. The $La_{0.8}Sr_{0.2}CoO_3$ target was purchased from MTI Corp., USA. The films were deposited at 650 °C under an oxygen pressure of 10 mTorr on the single crystalline $Yr_{0.08}Zr_{0.92}O_2$ (YSZ) substrates (MTI Corp., USA) with 20 nm $Gd_{0.2}Ce_{0.8}O_2$ interlayer grown with the same conditions as LSC films. The LSC film thickness was around 40 nm. After the growth process, the films were cooled down to room temperature in 2 Torr oxygen. To remove excess Sr and to deposit Ti at the surface of LSC thin films, the samples were dipped into the 2 mM $TiCl_4$ solution for 5–30 s at room temperature.[49,53] For samples which were not treated with Ti, the excess surface Sr-rich phase formed during the PLD process was removed by dipping of the films into a 0.1 M HCl aqueous solution for 10 s at room temperature.[54]

The Helios Nanolab 600 dual beam scanning electron microscope operated at a beam voltage of 15 keV and a current of 86 pA was used for imaging the surface morphology. A Veeco/Digital Instrument Nanoscope IV was used to perform tapping mode atomic force microscopy (AFM) for characterizing the surface morphology.

A Physical Electronics Model 700 scanning nanoprobe Auger electron spectroscopy (AES) instrument was used to identify lateral heterogeneities in cation compositions with high spatial resolution at the surface. Electron beam settings of 20 keV and 10 nA were used for both SEM imaging and the Auger electron excitation. The La MNN, Sr LMM, and Co LMM Auger emissions were measured for quantifying the surface cation composition of the LSC films. The sampling depths of these Auger electrons are ~8.0 nm for Sr LMM, ~4.0 nm for La MNN, and ~4.5 nm for Co LMM. The sampling depths for both the Auger and X-ray photoelectrons are estimated based on 3 times the inelastic mean free path (3× IMFP) of emitted electrons. However, we note that the Auger electron and photoelectron spatial profiles are exponentially dependent on the distance to the surface, so the data is always more sensitive to the near-surface region. It was not possible to quantify Ti due to low Ti content and overlapping of the most intense Ti Auger emissions with secondary Auger emissions of Sr and La. The smoothing and differentiation of the AES spectra collected were carried out using the Savitsky–Golay algorithm. Quantification of the AES differential spectra is

performed using peak-to-peak intensities of the tight-scans of the noted emissions from the constituent cations. The AES sensitivity factors were obtained by using the fractured surface of the LSC target as an internal standard of stoichiometry.

X-ray photoelectron spectroscopy (XPS) measurements have been performed in order to estimate the surface cation composition using a Perkin-Elmer PHI-5500 ESCA Spectrometer with monochromated Al Kα (1486.65 eV) X-ray radiation under a base pressure of 10^{-9} Torr. Angle-resolved XPS measurements were performed by changing the emission angle from 0° to 70° relative to the surface normal. The probing depth (3× IMFP) at 0° was 6 nm, 5 nm, 4 nm and 4 nm for Sr 3d, Ti 2p, La 3d, and Co 2p, respectively. Tilting the sample to the higher emission angle, α, decreases the effective probing depth by $\sin(\alpha)$. For example, tilting the sample to 70° decreases the probing depth down to 2.0, 1.7, 1.4, and 1.4 nm for Sr 3d, Ti 2p, La 3d, and Co 2p, respectively. The quantitative analysis of the Co 2p, La 3d, Sr 3d, and Ti 2p XPS spectra was performed using Multipack 9.0 software.

Electrochemical impedance spectroscopy (EIS) measurements were performed on asymmetrical cells with the LSC thin film electrodes grown on YSZ single crystal substrates. Dense platinum current collectors in the form of a grid (which covers 75% of electrode surface with 25 μm × 25 μm openings) were deposited on the LSC thin films by means of photolithography and RF sputtering. A porous Ag layer served as the counter electrode. Due to high electrical conductivity of LSC,[55,56] we do not expect a significant potential gradient across the LSC film from one Pt grid to the next. Furthermore, the key point of our paper is the chemical segregation process and its effect on the electrochemical performance. The stage of the experiments that involve surface cation segregation is simply annealing at open circuit voltage, so no effect of electrochemical potential is involved on the segregation itself in this work. A Parstat 2273 potentiostat was used to perform the EIS measurements in the frequency range of 100 kHz to 1 mHz with an AC amplitude of 5 mV and 0 V DC bias from 420 °C to 470 °C and to 520 °C in air. After measuring the EIS response of each film at a given temperature in air for 32 hours, the dependence of the surface exchange resistance on oxygen partial pressure was measured in the range of 1 atm to 10^{-3} atm at the same temperature. Then, the temperature was increased up to the next level and the same measurement sequence was repeated. ZView software was used for the data fitting and analysis.

Results and discussion

Surface morphology on the LSC films with chemical bath deposition of TiO_2

We examined the effect of Ti treatment on the surface morphology of LSC films by imaging these surfaces using scanning electron microscopy (SEM) and AFM. The XPS measurements at a 45° emission angle on the LSC-T films treated with $TiCl_4$ for 5, 10, 20 and 30 s have a Ti content of 2%, 6%, 10% and 13%, respectively, quantified as Ti/(La + Sr + Co + Ti) in their as-prepared state. These samples are denoted as LSC-T2, LSC-T6, LSC-T10, and LSC-T13. Even though surface roughness is relatively small and consistent among the samples (Fig. 1), it is comparable to the IMPF of the Ti photo-electrons measured in this work. Therefore, one can expect an underestimation of the actual Ti content compared to what it should be at the very top surface, especially for low takeoff angle measurements.

Thus, for quantification of Ti, we take the XPS results as "trends" and "lower bounds" rather than actual quantities.

Surface morphology of LSC-T2, T6 and T10 films is similar to that on LSC films treated only with HCl (Fig. 1a–c and e). As seen in the AFM images (Fig. 1a–c), these surfaces do not show any detectable Ti-induced morphological features. Thus, we hypothesize that the Ti is deposited in the form of either a thin and smooth wetting layer of Ti-oxide, or very small nanoparticles with sizes below the instrumental resolution of ~1 nm, or is dissolved into the surface lattice layer of the LSC film. This observation is also in line with the measured root mean square (RMS) roughness values which are almost the same for the LSC and the LSC-T2, LSC-T6 and LSC-T10 films. Further increase in Ti content up to 13% leads to an increase in the film RMS roughness. The increase of the film's roughness is also accompanied by the visible formation of the nanoparticles with a diameter of 3–10 nm at the LSC-T13 surface. It is likely that the particles observed on LSC-T13 are TiO_2.

Surface oxygen exchange kinetics over time

We compared the surface oxygen exchange coefficients, k^q, on LSC and LSC-T thin films as a function of time and temperature. We found that the stabilized k^q values of LSC-T films are 2–8 times higher than that of LSC at 420–530 °C, respectively, with the best results for LSC-T10. A typical impedance response of the cells with the LSC and LSC-T10 thin film electrodes, and the equivalent circuit[57,58] used for modeling the EIS data is shown in Fig. 2a. We obtained the surface polarization resistance, R_S, values from the low frequency impedance

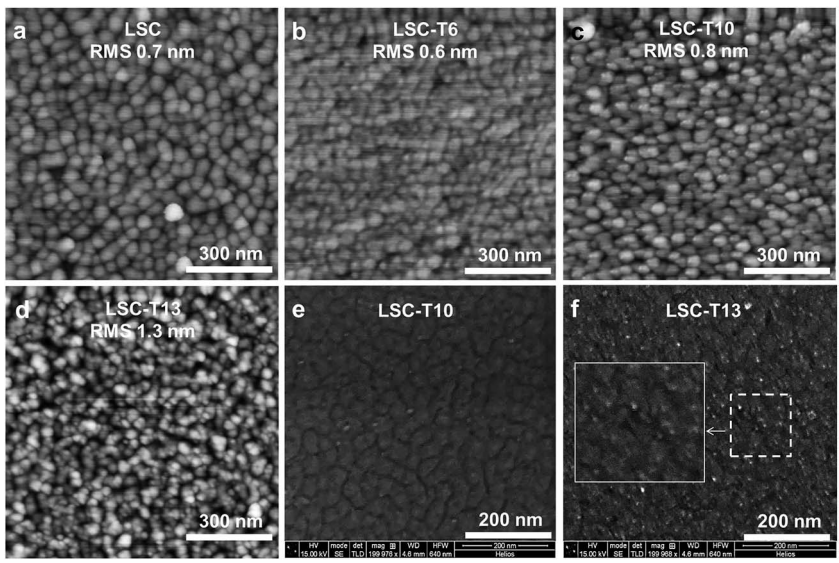

Fig. 1 Surface topography characterized by atomic force microscopy on (a) LSC, (b) LSC-T6, (c) LSC-T10, and (d) LSC-T13. Secondary electron microscopy images of (e) LSC-T10 and (f) LSC-T13 films. The inset in (f) marked with solid lines shows the magnified image of the area marked with the dashed lines.

response, and used those values to calculate the surface oxygen exchange coefficient, k^q, as:[59]

$$k^q = \frac{k_B T}{4e^2 c_0 R_S},$$

where k_B is the Boltzmann constant, T is the temperature, e is the electronic charge, and c_0 is the total concentration of lattice oxygen determined according to data from the study by Mizusaki *et al.*[60]

The measured k^q values as a function of time and annealing temperature are given in Fig. 2b. At the beginning, at 420 °C, all the samples have similar k^q values. Within the first few hours of annealing, the surface exchange kinetics degrades, and the k^q values decrease on all specimens. The LSC electrodes degrade most severely, with almost a one order of magnitude decrease of k^q within the first 30 hours at 420 °C. The stability of k^q improves by increasing the Ti content from 2% to 10% on LSC-T films. The LSC-T10 cathodes were the most stable and showed the highest k^q, which were 2 and 8 times higher than that on LSC at 420 and 530 °C, respectively. Increasing the Ti content from 10 to 13% degrades the stability of the LSC surface again. This loss in the improvement of stability can be related to the formation of small TiO_2 particles at the surface, as was shown in Fig. 1d and f. When the Ti content is in the range of 2–10%, the Ti-deposition uniformly wets and affects the LSC surface, preventing the degradation of the LSC-T. With the increase in Ti content, the TiO_2 at the surface is aggregated into nanoparticles (Fig. 1d and f), which may not provide complete surface coverage and cannot prevent surface degradation. We explain in the next section that the stability and improvement in the surface oxygen exchange kinetics is correlated to the relatively better stability of the surface cation chemistry.

Surface chemistry of LSC and LSC-T films at high temperature

In order to evaluate the changes in the surface cation chemistry and phase composition upon annealing at elevated temperatures, we performed combined

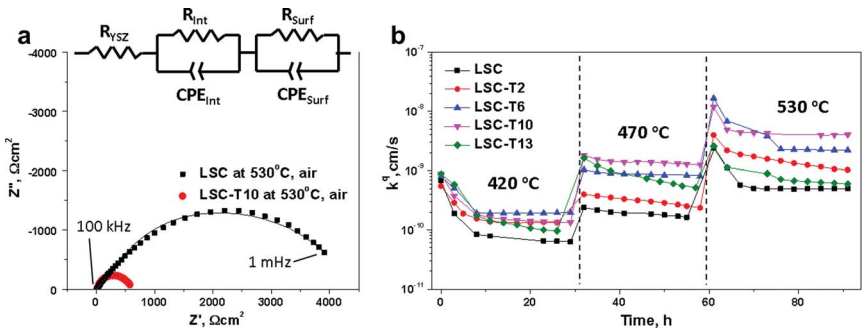

Fig. 2 (a) Representative electrochemical impedance spectra of the cells with the LSC and LSC-T10 thin film electrodes at 530 °C in air, and an equivalent circuit used to fit the experimental data adopted from ref. 53. Solid lines were obtained by fitting the equivalent circuit parameters to the data. (b) The oxygen surface exchange coefficient, k^q, over time at 420–530 °C, for LSC and LSC-T films with 2–13% Ti at the surface. Solid lines in (b) are a guide to the eye.

SEM and AES analysis on the LSC and LSC-T films. Sr-rich and Co-poor particles that were found at the surface of the films served as LSC cathodes. For the LSC, LSC-T2, and LSC-T13 films which demonstrated the lowest k^q, we found that the surfaces are largely covered with Sr-rich particles with sizes varying from several tens up to several hundreds of nanometers. The LSC-T10 surface which demonstrated the highest electrochemical performance and stability had significantly less particle coverage and higher Sr content within the particle-free (non-segregated) areas of the surface.

Fig. 3 shows the SEM images of the surface morphology on LSC and LSC-T films after annealing up to 530 °C in air. These are the same specimens whose surface exchange kinetics were measured by electrochemical impedance spectroscopy, as shown in Fig. 2. The average Sr/(Sr + La) and (Sr + La)/Co ratios deduced from the AES analysis on particles and on particle-free regions at the LSC and LSC-T surfaces are summarized in Table 1. While the as-deposited films (Fig. 1) had a homogeneous surface morphology and chemistry, the annealed LSC and LSC-T film surfaces show the presence of Sr-rich and Co-poor particles (Fig. 3). The segregated particle size varies from few tens up to several hundreds of nm. The Co content was lower and the Sr content was higher within particle-free zones compared to that on the as-fabricated LSC films or the particle-free zones of the annealed films, with the (Sr + La)/Co ratio in the particles measured as 2–3. Because of the difficulty of focusing the AES analysis volume due to sample drift and vibrations, the Sr/(La + Sr) and (Sr + La)/Co ratios on the particles reported in Table 1 should be taken as lower bounds to what the actual ratios should be on the particles. The LSC, LSC-T2, and LSC-T13 films which demonstrated the lowest k^q (Fig. 2) are largely covered with such Sr-rich particles (Fig. 3a, b and e). The LSC-T10 film, which has the fastest surface oxygen exchange kinetics (Fig. 2), had the most stable surface chemistry with the lowest coverage of the Sr-rich particles

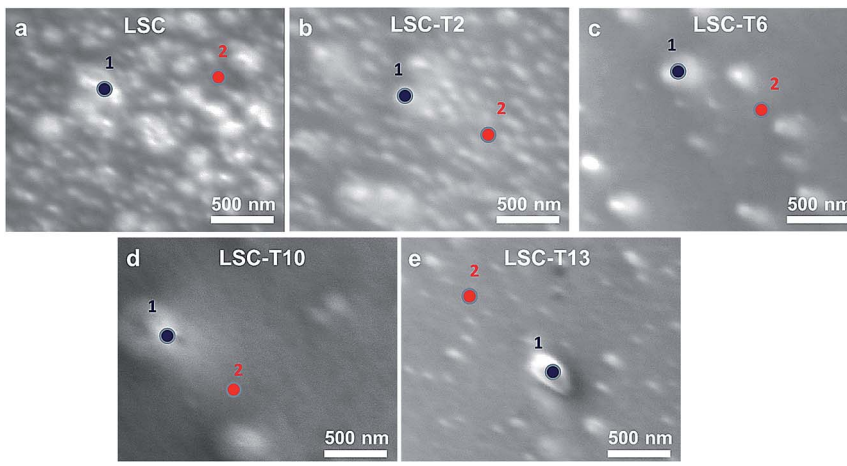

Fig. 3 Scanning electron microscopy images of the surface morphology of (a) LSC, (b) LSC-T2, (c) LSC-T6, (d) LSC-T10, and (e) LSC-T13 film cathodes after electrochemical testing up to 530 °C. Points 1 and 2 on each image indicate the particles and particle-free zones of the surface, respectively, where the chemical composition was probed by Auger electron spectroscopy as summarized in Table 1.

Table 1 Sr/(La + Sr) and (Sr + La)/Co ratios on particles and on particle-free regions on the LSC and LSC-T film cathodes after electrochemical testing at up to 530 °C. The values given in table are averages of several AES measurements at different points. The ± ranges represent the composition variations among different measurement points. The Sr/(La + Sr) and (Sr + La)/Co ratios are 0.20 ± 0.02 and 1.09 ± 0.09 respectively, on all the as-prepared samples before annealing and electrochemical testing up to 530 °C. Because of spatial resolution limits of the surface chemical analysis by the AES nanoprobe, the Sr/(La + Sr) and (Sr + La)/Co ratios on the particles should be taken as lower bounds

Sample	Sr/(Sr + La) (particle-free zone)	Sr/(Sr + La) (particle)	(Sr + La)/Co (particle-free zone)	(Sr + La)/Co (particle)
LSC	0.19 ± 0.02	0.51 ± 0.04	1.19 ± 0.10	2.1 ± 0.5
LSC-T2	0.16 ± 0.03	0.46 ± 0.06	1.30 ± 0.11	2.5 ± 0.9
LSC-T6	0.23 ± 0.02	0.66 ± 0.04	1.11 ± 0.07	2.6 ± 0.5
LSC-T10	0.25 ± 0.04	0.55 ± 0.04	1.04 ± 0.12	2.3 ± 0.5
LSC-T13	0.16 ± 0.04	0.43 ± 0.06	1.53 ± 0.11	2.8 ± 0.9

(Fig. 3d). This film also has a higher Sr fraction within the particle-free areas of the surface, indicating that a higher Sr fraction may remain within the LSC lattice. By combining the results shown in Fig. 2 and 3 and in Table 1, we conclude that the phase separated Sr-rich particles block the surface and increase its resistance toward ORR. This chemical and electrochemical stability at the surface of LSC is enhanced significantly by providing a small amount of Ti to the surface.

Mechanism behind the degradation of surface oxygen kinetics upon surface segregation

An evident effect of the segregated particles, as seen in Fig. 3, is the blockage of the LSC surface by an insulating Sr-rich phase that is inactive to ORR. In addition, formation of such Sr-rich particles decreases the Sr doping level within the LSC films. We expect that such a decrease of the Sr doping level within the near surface region of LSC reduces the availability of oxygen vacancies within LSC and slows down the ORR kinetics. To test this degradation mechanism, we performed measurements of k^q as a function of pO_2.

The double-logarithmic plots of the k^q *vs.* pO_2 for the LSC and LSC-T10 cathodes are given in Fig. 4. At 420 °C, the slope of the log–log plots for the LSC and the LSC-T10 cathodes are 0.38 and 0.43, respectively. These values are close to the previously reported slopes of k^q *vs.* pO_2 as 0.37–0.43 on LSC.[61,62] The overall reaction order of around 0.4 can be predicted from the contribution of individual reaction components.[61] According to mass action laws, a slope of 0.4 arises when the ORR rate limiting step depends on the availability of both the adsorbed oxygen species and of oxygen vacancies. If the rate determining step is governed only by availability of the adsorbed oxygen, the slope of k^q *vs.* pO_2 of 0.5 is expected. At the same time the oxygen vacancy concentration in LSC depends on pO_2 with a power of around −0.1.[60] By combining contributions from both the adsorbed oxygen species and the oxygen vacancy availability as reaction components, the overall reaction order of 0.4 can be deduced.

In the case of LSC in Fig. 4, we think that the change of the slope from 0.38 to 0.20 after annealing at higher temperatures is due to the increased effect of the oxygen vacancy availability as the rate limiting step. Indeed, previous studies on

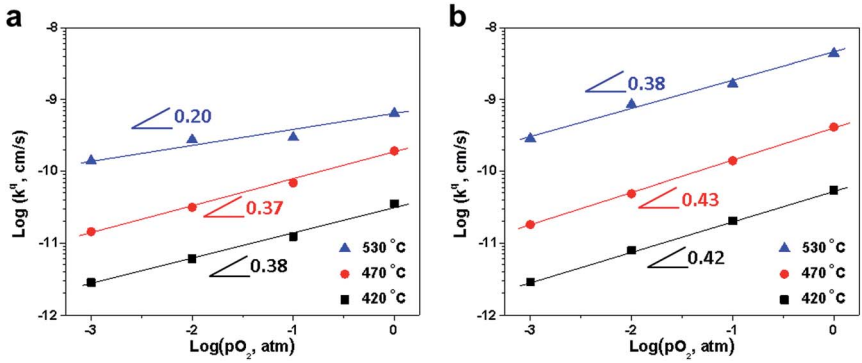

Fig. 4 The oxygen exchange coefficient, k^q, as a function of oxygen partial pressure, pO_2, for (a) LSC and (b) LSC-T10 cathodes at temperatures increasing from 420 °C to 530 °C. Before each pO_2 dependent measurement, the samples were kept at the corresponding temperatures for 32 h in air as shown in Fig. 2.

LSC showed that the power in the dependence of oxygen vacancy concentration on pO_2 becomes stronger with decreasing Sr fraction in LSC: from −0.06 for $La_{0.3}Sr_{0.7}CoO_3$ to −0.50 for $LaCoO_3$.[60] Thus, with the lowering of the Sr content within the LSC lattice upon Sr-rich particle separation (Fig. 3 and Table 1), the ORR rate limiting step, and consequently, k^q, depends more significantly on the oxygen vacancy availability. This effectively decreases the power in the dependence of k^q on pO_2 while slowing down the ORR kinetics at high oxygen partial pressure.

Ti distribution in LSC films

Fig. 5 shows the Ti content as a function of probing depth (photoelectron emission angle) for LSC-T10 in its as-fabricated conditions (described in Experimental section). It can be seen that even after annealing after 32 h, the Ti tends to stay

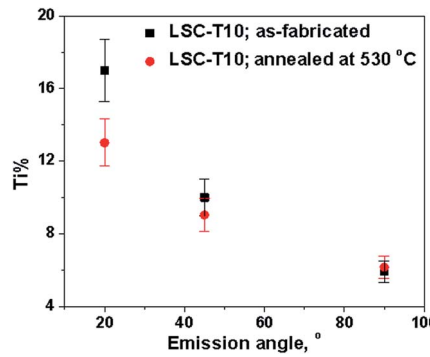

Fig. 5 Ti content quantified from the angle-resolved X-ray photoelectron spectroscopy measurements for the as-prepared LSC-T10 and after annealing at 530 °C in air for 32 h. Increasing the emission angle represents deeper probing depth from the surface. Error bars reflect 10% error generally associated with XPS measurements.

mostly at the film surface. However, there is some decrease in the Ti content at the very surface layer. A possible reason for this is the dissolution of Ti into the LSC lattice or the screening of Ti photoelectrons by the segregated particles at low angles of emission. More work is needed to uncover the exact coordination environment of Ti at the LSC surface.

Conclusion

We have shown that the chemical and electrochemical stability of the LSC surface can be improved by modifying the surface with Ti. Two different forms of surface modification were observed. When Ti content is below 10%, the deposited Ti stays in the form of a wetting layer, either dissolved into LSC, or in the form of a thin conformal TiO_2 layer. Higher Ti concentration leads to formation of dispersed TiO_2 nanoparticles at the surface. We found that the Ti surface content up to 10% (quantified by XPS) on LSC improved the surface oxygen exchange kinetics up to 8-fold by hindering the detrimental segregation of Sr-rich phases at 530 °C in air. The Sr-rich phase segregation slows the oxygen exchange kinetics, both by blocking the LSC surface with insulating particles and by decreasing the Sr-doping level and the oxygen vacancy availability within the LSC lattice. We believe that the presence of a small amount of Ti that dissolves into the LSC lattice at the surface decreases the oxygen vacancy concentration, and this effect decreases the electrostatic attraction of the negatively charged Sr'_{La} from bulk towards the LSC surface. As a result, the cation chemistry on LSC-T10 is more stable and gives rise to faster oxygen exchange kinetics. Ti-modification of the surface is proposed as one candidate for enabling better chemical stability and reaction kinetics on cobaltite based catalyst and electrocatalyst materials. In our ongoing work, we are investigating other surface compositions to systematically modulate the surface electrostatic driving force to segregation of the dopant cations.

Acknowledgements

The authors are grateful for the funding support from the NSF CAREER Award of the National Science Foundation, Division of Materials Research, Ceramics Program, Grant no. 1055583, from the US-DOE Basic Energy Sciences, Grant no. DE-SC00026333, and from the BP-MITEI Seed Project at MIT. The authors also acknowledge the use of the Center for Materials Science and Engineering, an MRSEC facility of NSF at MIT. This work made use of the MRSEC Shared Experimental Facilities at MIT, supported by the National Science Foundation under award number DMR-08-19762.

References

1 C. Graves, S. D. Ebbesen, M. Mogensen and K. S. Lackner, *Renewable Sustainable Energy Rev.*, 2011, **15**, 1–23.
2 E. V. Kondratenko, G. Mul, J. Baltrusaitis, G. O. Larrazabal and J. Perez-Ramirez, *Energy Environ. Sci.*, 2013, **6**, 3112–3135.
3 Z. Cai, M. Kubicek, J. Fleig and B. Yildiz, *Chem. Mater.*, 2012, **24**, 1116–1127.
4 Z. Cai, Y. Kuru, J. W. Han, Y. Chen and B. Yildiz, *J. Am. Chem. Soc.*, 2011, **133**, 17696–17704.

5 Y. Chen, W. Jung, Z. Cai, J. J. Kim, H. L. Tuller and B. Yildiz, *Energy Environ. Sci.*, 2012, **5**, 7979–7988.
6 E. J. Crumlin, E. Mutoro, S.-J. Ahn, G. J. la O', D. N. Leonard, A. Borisevich, M. D. Biegalski, H. M. Christen and Y. Shao-Horn, *J. Phys. Chem. Lett.*, 2010, **1**, 3149–3155.
7 S. Jiang, *J. Solid State Electrochem.*, 2007, **11**, 93–102.
8 W. Jung and H. L. Tuller, *Energy Environ. Sci.*, 2012, **5**, 5370–5378.
9 M. Kubicek, A. Limbeck, T. Frömling, H. Hutter and J. Fleig, *J. Electrochem. Soc.*, 2011, **158**, B727–B734.
10 E. Mutoro, E. J. Crumlin, M. D. Biegalski, H. M. Christen and Y. Shao-Horn, *Energy Environ. Sci.*, 2011, **4**, 3689–3696.
11 T. H. Shin, S. Ida and T. Ishihara, *J. Am. Chem. Soc.*, 2011, **133**, 19399–19407.
12 A. H. McDaniel, E. C. Miller, D. Arifin, A. Ambrosini, E. N. Coker, R. O'Hayre, W. C. Chueh and J. Tong, *Energy Environ. Sci.*, 2013, **6**, 2424–2428.
13 C.-Y. Tsai, A. G. Dixon, Y. H. Ma, W. R. Moser and M. R. Pascucci, *J. Am. Ceram. Soc.*, 1998, **81**, 1437–1444.
14 L. Yang, L. Tan, X. Gu, W. Jin, L. Zhang and N. Xu, *Ind. Eng. Chem. Res.*, 2003, **42**, 2299–2305.
15 E. Levi, A. Mitelman, D. Aurbach and M. Brunelli, *Chem. Mater.*, 2007, **19**, 5131–5142.
16 N. Yabuuchi, Y.-C. Lu, A. N. Mansour, S. Chen and Y. Shao-Horn, *J. Electrochem. Soc.*, 2011, **158**, A192–A200.
17 W.-S. Yoon, Y. Paik, X.-Q. Yang, M. Balasubramanian, J. McBreen and C. P. Grey, *Electrochem. Solid-State Lett.*, 2002, **5**, A263–A266.
18 S. W. Lee, C. Carlton, M. Risch, Y. Surendranath, S. Chen, S. Furutsuki, A. Yamada, D. G. Nocera and Y. Shao-Horn, *J. Am. Chem. Soc.*, 2012, **134**, 16959–16962.
19 D. Serrate, J. M. De Teresa, J. Blasco, M. R. Ibarra, L. Morellon and C. Ritter, *Appl. Phys. Lett.*, 2002, **80**, 4573–4575.
20 C. N. R. Rao and P. V. Vanitha, *Curr. Opin. Solid State Mater. Sci.*, 2002, **6**, 97–106.
21 S. Estrade, J. Arbiol, F. Peiro, I. C. Infante, F. Sanchez, J. Fontcuberta, F. de la Pena, M. Walls and C. Colliex, *Appl. Phys. Lett.*, 2008, **93**, 112505.
22 S. Estrade, J. M. Rebled, J. Arbiol, F. Peiro, I. C. Infante, G. Herranz, F. Sanchez, J. Fontcuberta, R. Cordoba, B. G. Mendis and A. L. Bleloch, *Appl. Phys. Lett.*, 2009, **95**, 072507.
23 I. Hamada, A. Uozumi, Y. Morikawa, A. Yanase and H. Katayama-Yoshida, *J. Am. Chem. Soc.*, 2011, **133**, 18506–18509.
24 F. Stavale, X. Shao, N. Nilius, H.-J. Freund, S. Prada, L. Giordano and G. Pacchioni, *J. Am. Chem. Soc.*, 2012, **134**, 11380–11383.
25 S. P. Jiang, *J. Solid State Electrochem.*, 2005, **11**, 93–102.
26 G. J. la O, S.-J. Ahn, E. Crumlin, Y. Orikasa, M. D. Biegalski, H. M. Christen and Y. Shao-Horn, *Angew. Chem., Int. Ed.*, 2010, **49**, 5344–5347.
27 J. Hayd, H. Yokokawa and E. Ivers-Tiffée, *J. Electrochem. Soc.*, 2013, **160**, F351–F359.
28 S. P. Jiang, *Solid State Ionics*, 2002, **146**, 1–22.
29 Z. Shao and S. M. Haile, *Nature*, 2004, **431**, 170–173.
30 Z. Cai, M. Kubicek, J. Fleig and B. Yildiz, *Chem. Mater.*, 2012, **24**, 1116–1127.

31 M. Kubicek, Z. Cai, W. Ma, B. Yildiz, H. Hutter and J. Fleig, *ACS Nano*, 2013, **7**, 3276–3286.
32 W. Lee, J. W. Han, Y. Chen, Z. Cai and B. Yildiz, *J. Am. Chem. Soc.*, 2013, **135**, 7909–7925.
33 H. Dulli, E. W. Plummer, P. A. Dowben, J. Choi and S. H. Liou, *Appl. Phys. Lett.*, 2000, **77**, 570–572.
34 H. Dulli, P. A. Dowben, S. H. Liou and E. W. Plummer, *Phys. Rev. B: Condens. Matter Mater. Phys.*, 2000, **62**, R14629–R14632.
35 J. Druce, H. Tellez, M. Burriel, M. D. Sharp, L. J. Fawcett, S. N. Cook, D. S. McPhail, T. Ishihara, H. H. Brongersma and J. A. Kilner, *Energy Environ. Sci.*, 2014, **7**, 3593–3599.
36 H.-S. Lee, C.-S. Park and H.-H. Park, *Appl. Phys. Lett.*, 2014, **104**, 191604.
37 R. Waser and M. Aono, *Nat. Mater.*, 2007, **6**, 833–840.
38 H. Jalili, J. W. Han, Y. Kuru, Z. Cai and B. Yildiz, *J. Phys. Chem. Lett.*, 2011, **2**, 801–807.
39 T. T. Fister, D. D. Fong, J. A. Eastman, P. M. Baldo, M. J. Highland, P. H. Fuoss, K. R. Balasubramaniam, J. C. Meador and P. A. Salvador, *Appl. Phys. Lett.*, 2008, **93**, 151904.
40 K. Katsiev, B. Yildiz, K. Balasubramaniam and P. A. Salvador, *Appl. Phys. Lett.*, 2009, **95**, 092106.
41 Y. Gong, D. Palacio, X. Song, R. L. Patel, X. Liang, X. Zhao, J. B. Goodenough and K. Huang, *Nano Lett.*, 2013, **13**, 4340–4345.
42 D. Lee, Y.-L. Lee, A. Grimaud, W. T. Hong, M. D. Biegalski, D. Morgan and Y. Shao-Horn, *J. Phys. Chem. C*, 2014, **118**, 14326–14334.
43 X. Zhu, D. Ding, Y. Li, Z. Lü, W. Su and L. Zhen, *Int. J. Hydrogen Energy*, 2013, **38**, 5375–5382.
44 A. Lussier, J. Dvorak, S. Stadler, J. Holroyd, M. Liberati, E. Arenholz, S. B. Ogale, T. Wu, T. Venkatesan and Y. U. Idzerda, *Thin Solid Films*, 2008, **516**, 880–884.
45 S. Estrade, J. Arbiol, F. Peiro, L. Abad, V. Laukhin, L. Balcells and B. Martinez, *Appl. Phys. Lett.*, 2007, **91**, 252503.
46 W. C. Chueh and S. M. Haile, *Annu. Rev. Chem. Biomol. Eng.*, 2012, **3**, 313–341.
47 M. M. Kuklja, E. A. Kotomin, R. Merkle, Y. A. Mastrikov and J. Maier, *Phys. Chem. Chem. Phys.*, 2013, **15**, 5443–5471.
48 N. Tsvetkov, L. Larina, O. Shevaleevskiy and B. T. Ahn, *Energy Environ. Sci.*, 2011, **4**, 1480–1486.
49 N. A. Tsvetkov, L. L. Larina, O. Shevaleevskiy, E. A. Al-Ammar and B. T. Ahn, *Prog. Photovoltaics*, 2012, **20**, 904–911.
50 B. Yildiz, N. Tsvetkov, and Q. Lu, U.S. Patent Application no.: 62/140009, 2015.
51 M. M. Islam, T. Bredow and A. Gerson, *Phys. Rev. B: Condens. Matter Mater. Phys.*, 2007, **76**, 045217.
52 Y.-L. Lee, J. Kleis, J. Rossmeisl, Y. Shao-Horn and D. Morgan, *Energy Environ. Sci.*, 2011, **4**, 3966–3970.
53 P. M. Sommeling, B. C. O'Regan, R. R. Haswell, H. J. P. Smit, N. J. Bakker, J. J. T. Smits, J. M. Kroon and J. A. M. van Roosmalen, *J. Phys. Chem. B*, 2006, **110**, 19191–19197.
54 M. Kubicek, A. Limbeck, T. Frömling, H. Hutter and J. Fleig, *J. Electrochem. Soc.*, 2011, **158**, B727–B734.
55 J. X. Wang, J. Shao, Y. K. Tao and W. G. Wang, *ECS Trans.*, 2009, **25**, 595–600.

56 E. Koep, D. S. Mebane, R. Das, C. Compson and M. Liu, *Electrochem. Solid-State Lett.*, 2005, **8**, A592–A595.
57 S. B. Adler, *Chem. Rev.*, 2004, **104**, 4791–4844.
58 J. Jamnik and J. Maier, *Phys. Chem. Chem. Phys.*, 2001, **3**, 1668–1678.
59 F. S. Baumann, J. Fleig, H.-U. Habermeier and J. Maier, *Solid State Ionics*, 2006, **177**, 1071–1081.
60 J. Mizusaki, Y. Mima, S. Yamauchi, K. Fueki and H. Tagawa, *J. Solid State Chem.*, 1989, **80**, 102–111.
61 R. E. van Doorn, I. C. Fullarton, R. A. de Souza, J. A. Kilner, H. J. M. Bouwmeester and A. J. Burggraaf, *Solid State Ionics*, 1997, **96**, 1–7.
62 P. Hjalmarsson, M. Søgaard and M. Mogensen, *Solid State Ionics*, 2008, **179**, 1422–1426.